Original

Jia, L.; Harbauer, K.; Bogdanoff, P.; Herrmann-Geppert, I.; Ramirez, A.;
van de Krol, R.; Fiechter, S.:

Alpha-Fe2O3 films for photoelectrochemical water oxidation – insights of key performance parameters

In: Journal of Materials Chemistry A (2014) Royal Society of Chemistry

DOI: 10.1039/c4ta04720f

Journal of Materials Chemistry A

PAPER

View Article Online
View Journal | View Issue

Cite this: J. Mater. Chem. A, 2014, 2, 20196

α-Fe_2O_3 films for photoelectrochemical water oxidation – insights of key performance parameters†

Lichao Jia,*[a] Karsten Harbauer,[a] Peter Bogdanoff,[a] Iris Herrmann-Geppert,[bc] Alejandra Ramírez,[a] Roel van de Krol[a] and Sebastian Fiechter[a]

Received 10th September 2014
Accepted 24th October 2014

DOI: 10.1039/c4ta04720f

www.rsc.org/MaterialsA

We report the deposition of ultra-thin α-Fe_2O_3 (hematite) films on fluorine-doped tin oxide (FTO) substrates using radio frequency (RF) sputtering, and the investigation of their photoelectrochemical (PEC) performance towards water oxidation. By varying the deposition pressure and time, the film microstructure and morphology could be optimized. The best hematite films having a thickness of about 50 nm exhibited a photocurrent density of 0.59 mA cm^{-2} at $U = 1.23$ V *vs.* RHE and 1.92 mA cm^{-2} at $U = 1.85$ V using a tungsten halogen lamp of 40 mW cm^{-2} light intensity in the wavelength range from 300 to 600 nm. These values are comparable or even higher than those ever measured hematite films (undoped and having no co-catalyst deposited on top of the electrode). Further measurements were explored to investigate the limiting factors in our films for possibly approaching their predicted PEC properties. A detailed analysis reveals that a slow water oxidation reaction and a trapping of charges on the surface, especially at the potential below 1.4 V, are obviously the reasons for the limited PEC performance.

Introduction

Photoelectrochemical (PEC) conversion of solar energy into chemical energy is an attractive yet challenging proposition, which offers the capability to efficiently produce hydrogen from water.[1] To design a PEC system, the choice of suitable photoelectrode materials is especially important because their electrochemical stability and their optoelectronic properties, such as the size of the band gap, the energetic positions of the valence and the conduction band, the optical absorption coefficient, the mobilities of electrons and holes and the lifetime of electron–hole pairs, determine the system's performance. A number of different semiconducting metal oxides have been studied for PEC water splitting.[2] Among them, hematite (α-Fe_2O_3) has emerged as a promising anode material and received much attention due to its suitable band gap of about 2.1 eV, an excellent chemical stability in a broad pH range, its natural abundance, nontoxicity and low cost. From the size of its band gap it has been predicted that this semiconductor can achieve a solar-to-hydrogen efficiency of about 12.8–16%, which corresponds to a maximum photocurrent of 12.6 mA cm^{-2} under AM 1.5G illumination (*i.e.*, 100 mW cm^{-2} light intensity).[3] Despite intense efforts, the reported water oxidation efficiencies for hematite to date are notoriously lower than the predicted maximum value.[4] This is caused by two limiting physical properties: the short lifetime of photogenerated charge carriers (<10 ps),[5] and the low mobility of the minority carriers (0.2 cm^2 V^{-1} s^{-1}).[6] The combined effect is that the minority carrier (hole) diffusion length is only 2–4 nm,[7] whereas full absorption of the incident light requires much thicker films due to the indirect nature of the bandgap (penetration depth of light is ~118 nm at a wavelength of 550 nm). Furthermore, the slow kinetics of the oxygen evolution reaction at the surface of the oxide limit the overall performance of the material.[8] Finally, the conduction band energy is located ~0.4 eV below the H_2/H^+ redox energy, which means that hydrogen evolution is only possible when an additional bias voltage is provided, or when the n-type α-Fe_2O_3 electrode is combined with a p-type photocathode, for example Cu_2O.

Ultra-thin films of ≤50 nm thickness deposited on a conductive substrate should facilitate the transport and collection of electrons and holes at the front and back contact of the film after optical excitation. However, such thin films do not allow for sufficient absorbance of visible light, which limits the PEC efficiency. Developing new strategies to balance the optical absorption and the transport of excited charge carriers to the

[a]Helmholtz-Zentrum Berlin für Materialien und Energie, Institute for Solar Fuels, Hahn-Meitner-Platz 1, 14109 Berlin, Germany. E-mail: Lichao.jia@helmholtz-berlin.de

[b]Helmut-Schmidt-University Hamburg, Functional Materials, Holstenhofweg 85, 22043 Hamburg, Germany

[c]Helmholtz-Zentrum Geesthacht – Centre for Materials and Coastal Research, Max-Planck-Str. 1, 21502 Geesthacht, Germany

† Electronic supplementary information (ESI) available: Complementary Raman spectra, XPS, UV-Vis, SEM, XRD and DEMS for the catalyst. See DOI: 10.1039/c4ta04720f

electrode/electrolyte interface and to the back contact, respectively, is therefore an important part of ongoing efforts to achieve high performance hematite-based PEC cells. To address the slow oxygen evolution kinetics, a catalyst and/or a buffer layer, which is usually deposited on the film's surface, can effectively passivate surface states and improve the charge transfer kinetics at the absorber/catalyst or the electrode/electrolyte interface. For example, an ultrathin Al_2O_3 passivation layer deposited by atomic layer deposition was found to reduce the overpotential of the oxygen evolution reaction (OER) of hematite photoanodes by around 100 mV and increase the photocurrent by a factor of 3.5 at 1.0 V_{RHE} due to a passivation of surface states.[9] In addition, functionalizing the hematite surface by an IrO_2 catalyst evokes an increase in the saturation current density of around 20% at 1.23 V_{RHE} due to an additional cathodic shift in the onset potential of the *I–V* curve by around 0.2 V.[10] The electrodeposition of a Co–Pi catalyst on the surface of the hematite films also results in a cathodic shift of the photocurrent onset potential by more than 100 mV and an increase the saturation photocurrent density by around 100 μA cm^{-2} at 1.4 V_{RHE}.[11] However, the modified samples always suffer from the problem of instability during PEC water splitting in the required strongly basic electrolyte. Two other main approaches have been pursued to overcome the trade-off between charge carrier transport and photon penetration depth: one is to develop nanostructures based on host scaffolds–guest absorbers,[12a] and another one is to use resonant absorption in ultrathin smooth films with reflecting back-contacts (light trapping).[12b] An extremely thin hematite film coated on a high surface area host scaffold has been described as a promising route, because the photoexcited carriers are generated within the range of the carrier diffusion length which allow most photoexcited carriers to reach the surface before recombining. However, preparation of host scaffold–guest absorber structures is complex and time-consuming, and the usual preparation techniques (such as spray pyrolysis, APCVD, and ALD) rely on highly reactive, flammable, toxic and expensive metal–organic compounds. This drives the search for alternative facile, safe, and cost-effective strategies to fabricate ultra-thin nanostructured α-Fe_2O_3 films with high PEC performance.[13]

In this work, we present a simple radio frequency (RF) sputtering deposition technique for the fabrication of transparent, ultra-thin and nanostructured α-Fe_2O_3 films on a conducting glass substrate using a Fe_2O_3 target. This technique offers the synthesis of hematite films with controlled particle size and film thickness by varying deposition pressure and deposition time. Nevertheless, sputtering of hematite takes the risk of a partial decomposition of the oxide into the iron spinel phase magnetite. Therefore, fine tuning of the sputter parameters is needed to guarantee phase pure hematite film formation. In this contribution it has been demonstrated that the preparation of hematite films by sputtering is feasible. Even without the addition of a catalytic coating or interfacial layer, these ultra-thin (∼50 nm) hematite photoanodes show a water oxidation photocurrent density of 0.59 mA cm^{-2} at 1.23 V *vs.* RHE. Above 1.23 V the slope of the *U–I* curve flattens, resulting in a photocurrent of 1.92 mA cm^{-2} at $U = 1.85$ V before the dark current onset. Furthermore, from the performed PEC studies it can be concluded that the films suffer from slow water oxidation kinetics and electron surface trap states which limit the photoresponse of the films.

Experimental

Hematite thin film preparation

Fluorine-doped SnO_2 (FTO) substrates were employed as transparent supports. α-Fe_2O_3 films were deposited from a pure hematite target on FTO substrates by radio frequency (RF) magnetron sputtering at room temperature. Before deposition, all substrates were cleaned by sonication in acetone, ethanol, and finally water and dried in an N_2 gas flow afterwards. The deposition of α-Fe_2O_3 was performed in a homemade sputtering and evaporation system (basic pressure 4×10^{-6} Pa). The Fe_2O_3 sputter target (3 inch diameter, 99.95% purity) was pre-sputtered for five minutes before reactive sputtering onto FTO substrate was started. The distance between the sputter target and the substrate was 66 mm for all depositions. The sputter plasma was generated at a constant power of 50 W. The purity of the Ar gas was 99.99%. After deposition the samples were annealed in air at 800 °C for 10 minutes.

Film characterization

The morphology of thin hematite films were characterized using a high-resolution scanning electron microscope (LEO 1530 from Zeiss). The crystal structure was determined by X-ray diffractometry (XRD) using a D8-Advanced Bruker diffractometer with a Cu-Kα X-ray source in Bragg–Brentano geometry. Raman spectra were acquired using a LabRam spectrometer (Horiba Jobin Yvon) at room temperature with He/Ne laser (632.8 nm) as excitation source. Optical behavior was determined using a UV-Vis spectrometer (Lambda 950, Perkin-Elmer) with a 150 mm InGaAs integrating sphere and spectrolon as standard for 100% reflectance.

Photoelectrochemical measurements

Photocurrent measurements were performed to determine the solar photocurrent of the photoanodes in a three-electrode compartment (EG&G, 273A). 1 M KOH aqueous solution of pH 13.6, a Pt wire, and an Hg/HgO electrode were employed as electrolyte, counter electrode, and reference electrode, respectively. A tungsten halogen lamp (Xenophon) was used as light source. The lamp was adjusted to a light intensity of 40 mW cm^{-2} related to the wavelength range from 300 to 600 nm fitting to the light absorption of hematite. This intensity is close to the value of solar light in the related wavelength range corresponding to an intensity 30 mW cm^{-2}. However, we have to note that the spectral distribution of the light differs from AM1.5.

All measurements were performed illuminating the films *via* the electrolyte to investigate the hematite–electrolyte interface and *via* the transparent conductive oxide through a 0.32 cm^2 mask that defines the electrode area exposed to the electrolyte and the light. The potential of the hematite photoanodes was swept at a scan rate of 10 mV s^{-1} from cathodic to anodic

potentials. The potential was converted to the reversible hydrogen electrode (RHE) potential. The differential electrochemical mass spectroscopy (DEMS) was designed to simultaneously measure released gases during an electrochemical measurement. All of the electrochemical data shown here were not iR corrected, and the Faradaic efficiency is 100%.

Results and discussion

The as-deposited films only show very small and broad X-ray diffraction (XRD) peaks, indicating the mainly nano-sized/amorphous nature of the films. After annealing, crystallization of the hematite phase is noticed, and a preferred orientation of the grains along the hexagonal *c*-axis parallel to the substrate has been observed (Fig. 1a). Besides the ⟨110⟩ and the ⟨104⟩ hematite peaks, no peaks other than those belonging to the fluorine-doped tin oxide (FTO) substrate were found, which is consistent with the results reported by other authors using different deposition methods.[4a–f,14] This indicates that the (110) planes of the deposited film could be oriented parallel to the substrate and the (001) planes belonging to the same particle could be standing perpendicular to it. As is well known, hematite possesses a strongly anisotropic conductivity, which is up to four orders of magnitude higher within the (001) basal planes than in [001] direction.[15] Therefore, it is expected to facilitate the charge carrier transport to back and front contact of the films.

In addition to XRD measurements, the Raman spectrum shown in Fig. 1b confirms the presence of α-Fe_2O_3 in the films. In the range from 200 to 1500 cm^{-1}, numerous peaks are visible. All the significant peaks (expect the peaks at 660 and 1090 cm^{-1}) can be indexed as α-Fe_2O_3.[16] The Raman peaks

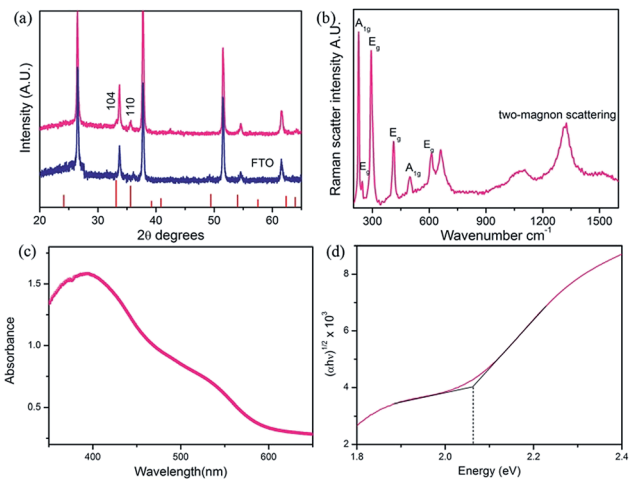

Fig. 1 X-ray diffraction pattern (a) and Raman spectrum (b) of a hematite film obtained by radio frequency sputtering and subsequent annealing (deposition time 60 min, pressure 0.3 Pa). The red lines in (a) represent the standard power diffraction pattern of hematite according to JCPDS 89-0597. (c) UV-Vis absorbance *A* of the hematite, which was corrected with respect to reflection *R* according to the equation $A = -\log[T/(1-R)]$; (d) Tauc plot of an absorption spectrum of a typical hematite film indicating an indirect band gap.

appearing at 225 and 498 cm^{-1} are assigned to the A_{1g} mode, and those at 245, 292, 405, and 611 cm^{-1} to Eg modes. The peak located at 1320 cm^{-1} is assigned to hematite due to two-magnon scattering which arises from the interaction of two magnons created by adjacent spin sites with antiparallel orientation. The weak peak around 1090 cm^{-1} was also found by other authors, but was normally not mentioned because of the lack of a convincing assignment.[17] The peak at 660 cm^{-1} is tentatively attributed to a feature belonging to magnetite (Fe_3O_4) which has a strong Raman band exactly at this value. Small magnetite inclusions in the films could be the reason for the appearance of this peak.[16] Another explanation for this observation is the presence of a disordered hematite phase, as described previously for hematite powder.[18a] It is thought that such a disorder could be induced by the small grain size in our films. This assumption is consistent with the fact that the 660 cm^{-1} peak intensity decreases after high-temperature annealing of our samples (Fig. S1a†). Additionally, XPS results shown in Fig. S1b† present that in our film there is only Fe_2O_3, no any peaks from Fe_3O_4 can be detected.[18b] Thus, the disordered Fe_2O_3 phase at 660 cm^{-1} in Raman spectrum can be further confirmed.

The optical properties of the annealed hematite film are characterized by UV-Vis spectroscopy (Fig. 1c). An increase of absorption occurs just below 600 nm, indicating a band gap of about 2.06 eV (see Fig. 1d), which is consistent with the results reported by other researchers.[19] The slow increase of the absorbance is typical for an indirect band gap.[4a,14] The peak position in the optical curve at around 400 nm and the turning point at 540 nm are assigned as an indirect electronic transition within the d-states of Fe^{3+} ions and a direct transition from O^{2-} p to Fe^{3+} d states, respectively.[4c] This optical behaviour is typical for the optoelectronic properties of hematite. Furthermore, the absorption does not go to zero above 600 nm, which means that some degree of light scattering occurs in our samples.

Representative top-view Field Emission Scanning Electron Microscope (FESEM) images of the sample deposited on FTO at 0.3 Pa pressure for 60 min are presented in the Fig. 2a and b. As seen from the top view SEM image (Fig. 2a), the film is uniform and homogenous. Apparently, this dense film consists of large globular or oval particles with sizes ranging from 150 nm to 400 nm. Each particle shown is composed of smaller grains. It is worth to note that the surface of the film has a high roughness, which cannot be ascribed to the SnO_2 substrate since the latter has much larger crystallite grains. The cross section in Fig. 2b demonstrates that the hematite film forms continuous coatings on the FTO substrate. Further, cross section transmission electron microscopy (TEM) (Fig. 2c) shows that the film has a thickness of about 50 nm. A typical columnar grain structure can be observed in Fig. 2d, with sizes of the individual grains in the range from 30 to 40 nm. The columns in the films are vertically oriented to the substrate, with at most one grain boundary between the film surface and the back-contact. This morphology is clearly favourable for the transport of excited charge carriers in the film. The TEM images also once again indicate a conformal and dense coverage of the FTO layer by the

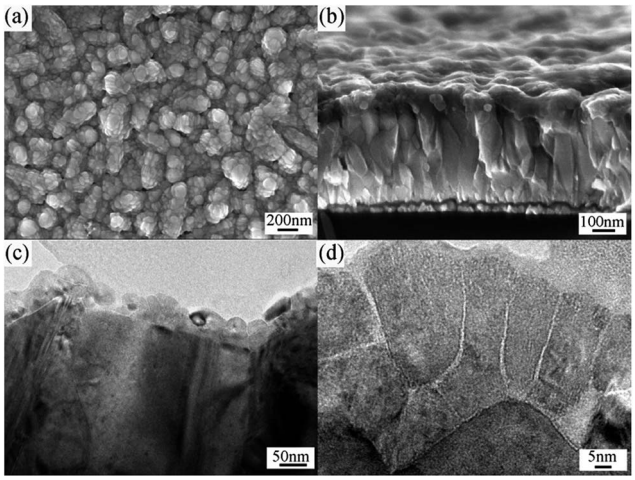

Fig. 2 Field Emission Scanning Electron Microscope (FESEM) top view images (a) and cross section (b) of an α-Fe_2O_3 film obtained by radio frequency sputtering and subsequent annealing (deposition time 60 min, pressure 0.3 Pa). (c–d) The corresponding Transmission Electron Microscope (TEM) cross section images of (a) and (b).

hematite nanoparticles. This is essential in order to avoid a short circuit between the FTO and the electrolyte. Such a short circuit would result in large background (dark) currents, and can substantially decrease the performance of the hematite photoanode. As mentioned above, the Raman spectra suggest that the deposited films could partially consist of a disordered hematite phase. This observation is supported by the fact that the particle size of homogeneously X-ray scattering crystallites is smaller than the thickness of the layers. Using Scherrer's equation, a mean particle size of about 20 nm is calculated from the X-ray pattern of Fig. 1a.

PEC measurements were performed in a three-electrode electrochemical cell using nanostructured hematite films deposited on FTO glass as the working electrode, a platinum wire as counter, and a mercury–mercurous sulfate electrode as reference electrode. The photocurrent density *vs.* potential curve of the hematite photoanodes after annealing of the layers at 800 °C for 10 minutes (short enough to prevent melting of the FTO glass) is presented in Fig. 3a. The measurements were performed in 1 M KOH electrolyte (pH 13.6). The potential of the hematite photoanodes was swept with a scan rate of 10 mV s^{-1} from cathodic to anodic potentials in the dark and under front- and back-side illumination. The dark response (dashed line in Fig. 3a) is negligible up to about 1.8 V *vs.* RHE, after which direct oxidation of water sets in due to the formation of an inversion layer.[4a] At potentials positive of 1.0 V_{RHE}, a pronounced photocurrent is observed when the electrode is illuminated. The water oxidation photocurrent rises to 0.59 mA cm^{-2} at 1.23 V *vs.* RHE, reaching a maximum of 1.92 mA cm^{-2} at ~1.8 V before the onset of the dark current. To the best of our knowledge, these values are comparable or even higher than that ever measured so far on sub-50 nm films of pure (undoped) Fe_2O_3 films without any water oxidation catalyst deposited on top.[13,20]

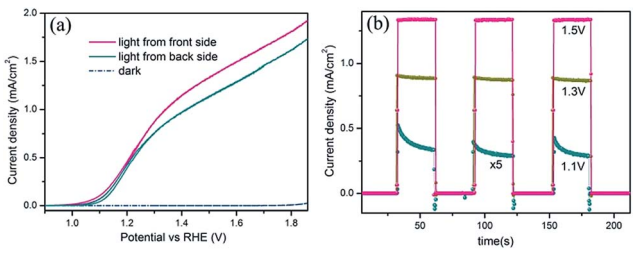

Fig. 3 (a) Current densities *vs.* voltage curves of sample shown in Fig. 2(a) in darkness (dashed line), under front side and back side illumination (solid lines) using a W–I lamp (40 mW cm^{-2}), (b) transient photoresponse shown by light chopping current densities (light on and light off) as a function of time. Different bias potentials (1.1, 1.3, 1.5 V *vs.* RHE) were applied as indicated.

To approach possible the predicted PEC properties and to design an effective strategy for improving the performance, the rate-limiting steps of charge transfer have first been elucidated by comparing the photocurrent behaviour after illumination from the front and the back side of the films. Due to the low absorption coefficient of hematite, photons having an energy larger than the band gap of the oxide generate electron–hole pairs everywhere in the volume of the film. Since the film is nominally undoped, the donor density is presumably less than 10^{18} cm^{-3} and the space charge width can extend throughout the entire thickness of the film. If this is indeed the case, the minority carrier diffusion length (2–4 nm) (ref. 7) no longer limits the collection length of the carriers, and charge carriers generated in the bulk can also contribute to the photocurrent. As shown in Fig. 3a, the photocurrent density for back side illumination is nearly the same as that for front side illumination at 1.23 V, indicating that the mobility of carriers is not the limiting factor of the PEC performance in our hematite films. At higher bias potentials however, the photocurrent under front illumination exceeds the corresponding photocurrent under back illumination. Obviously, in general the electrons seems to have a higher mobility compared to the hole mobility. Actually, the superior transport of photo-excited electrons to the back contact can easily be understood due to the preferential orientation of the hematite lattice planes in the grains of the columnar grown films (see XRD and TEM cross section micrographs).

It can be assumed that the photocurrent observed under illumination is a direct measure of the water splitting rate, and that it reflects the number of charge carriers produced by the incident light and their subsequent participation in the water oxidation reaction. For a better understanding of the photoresponse of our films, chronoamperometric (current density *vs.* time) experiments were carried out at different applied bias potentials, as displayed in Fig. 3b. The photocurrent taken at 1.5 V adopts a steady state value within less than 2 seconds after starting the illumination. As soon as the illumination is interrupted, the current rapidly drops to zero, with no discernible overshoot to negative currents. Very similar behaviour is observed at the curve taken at 1.3 V but here a very low decline (transient) of the photocurrent is observed. Nevertheless, these results suggest that there is no significant charge accumulation by holes at the electrode/electrolyte interface, implying fast charge transport and injection kinetics to the OER caused by a

sufficiently high bias potential and band bending of the space charge layer. Limiting processes for the performance seem to be rather originating from recombination processes in the bulk. In contrast to that at a potential of 1.1 V *vs.* RHE (the current density in Fig. 3b is enlarged by a factor of five for a better visualization of the transient), a large decline of the photocurrent is observed on a time scale of tens of seconds after turning on the light. This indicates accumulation and thereby also recombination of holes at the hematite–electrolyte interface due to either slow water oxidation kinetics and/or filled electron surface trap states.[21] Upon turning the light off, no corresponding negative photocurrent transient can be observed. Instead of this only a fast negative current spike is monitored. Obviously, only a very small fraction of accumulated holes recombine in a fast time domain with electrons from the external current circuit. The main fraction of accumulated holes seems to recombine with electrons which are trapped in surface states (as shown in Fig. 4a). Therefore no current occurs in the external current circuit. The negative charge of these trapped electrons could also be responsible for the suppressed recombination process with electrons from the external circuit. With increasing bias potentials the decline of the photocurrent transients decreases (see Fig. 3b, at 1.3 V *vs.* RHE) and finally nearly disappears (see Fig. 3b, at 1.5 V *vs.* RHE), indicating that accumulation of holes is almost eliminated and all holes arriving at the surface can participate in the water oxidation reaction. This is achieved by a higher reaction rate of the OER at higher overvoltages and by a stronger band bending which diminishes the probability of trapped electrons in surface states.

These results are in accordance with measurements performed in the presence of the hole scavenger H_2O_2 as shown in Fig. 4b. Furthermore, once 0.1 M H_2O_2 was added to the electrolyte, the onset potential shows a negative shift of around 300 mV and a large increase in the photocurrent is observed at potentials lower than 1.4 V. This is a clear evidence that the slow water oxidation kinetics limit the photoresponse of these hematite photoanodes. To improve this, co-catalysts need to be deposited on the electrode surface, such as IrO_2, Co–Pi, Co–Mn, CoO_x, Ru–abd and so on.[10,11,22] In contrast, at a bias potential of 1.5 V no improvement of the photocurrent can be achieved by adding H_2O_2, so that the OER kinetics seem not to be the bottleneck of the overall efficiency and recombination processes in the bulk have to be considered.

In order to track the gaseous species produced during the water oxidation, differential electrochemical mass spectroscopy (DEMS) measurements were performed. As displayed in Fig. S2,† the onset of the oxygen mass signal under illumination occurs at a voltage of 1.0 V_{RHE}, which corresponds well to the onset of the photocurrent. The signal steeply increases with increasing voltage, indicating the instantaneous oxygen evolution reaction at the electrode/electrolyte interface of our sample. The stability of hematite photoanodes was performed at a potential of 1.23 V *vs.* RHE (Fig. S3†). The photocurrent did not shown any decrease after 60 min, indicating that the hematite film does not contain any unstable species or phases.

The efficiency of the hematite film is likely to depend strongly on its microstructure, such as the presence of grain boundaries and its crystallographic orientation.[23] To investigate these aspects, we modified the deposition pressure and deposition time to see how this affects the PEC performance. Films of approximately equal thickness, but deposited with different sputter pressures (0.2, 0.3, 0.5 and 0.8 Pa) are first evaluated using cyclic voltammetry (CV) as a characterization tool. The photocurrent densities for all photoelectrodes are plotted against the potential *vs.* RHE as presented in Fig. S4.† The films exhibit markedly different photoactivities at different deposition pressures. The variations can be clearly seen in Fig. 5a, where the photocurrent density at 1.23 V *vs.* RHE is plotted against the deposition pressure. With increasing deposition pressure, the photocurrent initially increases to a maximum value of 0.59 mA cm^{-2} at 0.3 Pa, and then decreases to less than 0.1 mA cm^{-2} at 0.8 Pa. This suggests that the photocurrent is strongly correlated with the microstructure of the film (including particle size and crystallographic orientation of the grains).

But also other influences such as the oxygen activity at the surface cannot be excluded. The initial increase of photocurrent can be ascribed to the increased crystallinity within the film, as illustrated by the increase of the XRD peak intensities of the main reflections ⟨110⟩ and ⟨104⟩ of Fe_2O_3 at a sputter pressure of 0.3 Pa (see Fig. S5†). At higher sputter pressures the full width half maxima of these main peaks decrease and the ratio of the XRD peaks approaches the value of randomly oriented hematite particles (compare the size of the diffraction bars of the

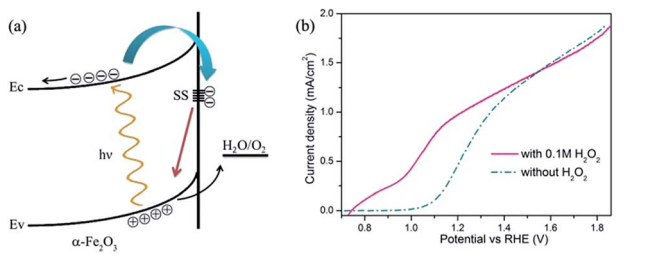

Fig. 4 (a) Schematic drawing illustrating trapped electrons at the hematite–electrolyte interface and their recombination with holes generated under illumination; (b) current densities *vs.* voltage curves of sample shown in Fig. 2a in either 1 M KOH or 1 M KOH with H_2O_2 using a W–I lamp (40 mW cm^{-2}).

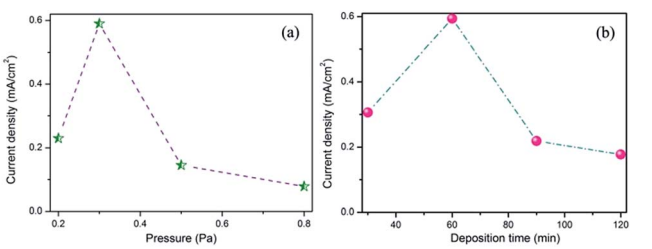

Fig. 5 (a) Photocurrent densities at 1.23 V_{RHE} as a function of deposition pressure; (b) photocurrent densities measured at 1.23 V_{RHE} as a function of deposition time.

hematite XRD reference pattern in Fig. S5† with the measured peak heights of the films with increasing sputter pressure). Although the hematite grains have now a size of at least 30 nm as determined by Scherrer's equation, the PEC performance of the layer sputtered at 0.8 Pa is the poorest. Additionally, particle growth could also be confirmed by top view SEM images displayed in Fig. S6.† The images indicate that by increasing the sputter pressure from 0.3 Pa to 0.8 Pa the size of particles gradually increases. Larger particles mean that the carriers have to diffuse over longer distances in these films resulting in a lower photocurrent at higher pressures. However, this does not play an important role due to the presence of the space charge layer across the entire thickness of the hematite film. However, the statistic distribution of the larger grains in the films deposited at a sputter pressure of 0.8 Pa compared to a textured film deposited at 0.3 Pa could be the reason for a reduced current density because a film of random grain distribution transport of electron and holes should be less favorable than in an 11.0 textured film.

In order to investigate the effect of film thickness on photon absorption and photocurrent generation, a number of films were prepared at 0.3 Pa while varying the deposition time. Since the deposition rate is 0.83 nm min^{-1} at a sputter power of 50 W (checked by Dektak surface profiler) and a deposition pressure of 0.3 Pa, the thickness of each film can easily be calculated. Films deposited for 30, 60, 90 and 120 min therefore should result in films with a thickness of about 25, 50, 75 and 100 nm. The UV-Vis spectra presented in Fig. S7† show similar absorption features (*i.e.* onset of band gap transition). As expected the absorbance increases linearly with increasing film thickness. The current–potential curves of films with different thickness are shown in Fig. S8.† The photocurrent steadily increases until the film has attained a thickness of 50–60 nm. Further increase of the hematite film thickness results in the reduction of the photocurrent density, as illustrated in Fig. 5b. Starting with a photoelectrode of 25 nm film thickness, the poor light harvesting of the film limits the number of electron–hole pairs generated. A further increase of the layer thickness significantly increases the photocurrent density (*e.g.* at 1.23 V *vs.* RHE) from 0.3 mA cm^{-2} for the photoelectrode with 25 nm thickness to 0.59 mA cm^{-2} for a layer of about 50 nm thickness. The linear increase in photocurrent is thus considered mainly due to an augmented amount of deposited photoactive material, which enhances the light absorption as well as the total number of photoexcited carriers. As soon as the film thickness exceeds 50 nm, the photocurrent dramatically drops back to 0.2 mA cm^2 which can be explained by the presence of a higher number of grain boundaries across the film thickness in thicker films. Longer diffusion distances cannot explain this effect due to the presence of a space charge layer extending over the thickness of the film. On the one hand a thick film can absorb more incident photons resulting in a higher number of excited electron–hole pairs, but the excited charges are lost by recombination processes in the bulk and at grain boundaries migrating from the front to the back contact and *vice versa*.

Conclusions

In summary, thin α-Fe_2O_3 films with columnar structure were successfully deposited onto FTO substrates by magnetron sputtering. Detailed analysis of the structural, optoelectronic and photoelectrochemical properties of films deposited under different sputter conditions revealed that under optimized conditions the columns in the films are 11.0 textured and consist of one grain extending from the film's surface to the back-contact, which is favorable for the transport of excited charge carriers in the film. By varying the deposition parameters such as sputter pressure and deposition time, the film thickness, the morphology and the crystallinity of the films have been tuned. All these parameters are closely correlated with the PEC performance. It was found that films with a thickness of approximately 50 nm thickness deposited at a sputter pressure of 0.3 Pa for 60 min possess the highest photocurrent density of 0.59 mA cm^{-2} at 1.23 V_{RHE} and 1.92 mA cm^{-2} at 1.8 V_{RHE} using a W–I lamp (40 mW cm^{-2}). Further electrochemical measurements were undertaken to tackle the limiting factors of these films. The chronoamperometric experiments and the comparison of the photocurrent behavior from the front and back side indicated that surface trapping states is one of the bottlenecks for acquiring high PEC efficiency. In addition, measurements in the presence of the hole scavenger H_2O_2 revealed the slow water oxidation kinetics of the films. Therefore, it is highly expected that co-catalysts such as IrO_2, Co–Pi, Co–Mn, CoO_x and a surface treatment (such as plasma etching or ozone treatment) could be used to further improve the performance of these hematite films in our future work.

Acknowledgements

This work was supported by the German Federal Ministry of Education and Research (BMBF) under contract # 03SF0353A "H_2-NanoSolar". The authors like to thank Mrs Ulrike Bloeck for the preparation of cross section samples and taking TEM images.

Notes and references

1 (*a*) Á. Valdés, J. Brillet, M. Grätzel, H. Gudmundsdóttir, H. Hansen, H. Jónsson, P. Klüpfel, G. Kroes, F. Formal, I. Man, R. Martins, J. Nørskov, J. Rossmeisl, K. Sivula, A. Vojvodic and M. Zäch, *Phys. Chem. Chem. Phys.*, 2012, **14**, 49; (*b*) K. Maeda and K. Domen, *J. Phys. Chem. Lett.*, 2010, **1**, 2655; (*c*) J. Sun, D. Zhong and D. Gamelin, *Energy Environ. Sci.*, 2010, **3**, 1252; (*d*) R. van de Krol, Y. Liang and J. Schoonman, *J. Mater. Chem.*, 2008, **18**, 2311.

2 (*a*) T. Takashima, K. Hashimoto and R. Nakamura, *J. Am. Chem. Soc.*, 2012, **134**, 1519; (*b*) T. Nakajima, T. Nakamura, K. Shinoda and T. Tsuchiya, *J. Mater. Chem. A*, 2014, **2**, 6762; (*c*) H. Q. Wang, L. C. Jia, P. Bogdanoff, S. Fiechter, H. Möhwald and D. Shchukin, *Energy Environ. Sci.*, 2013, **6**, 799; (*d*) A. Deshpande, S. Kelkar, S. Rayalu and S. Ogale, *J. Mater. Chem. A*, 2014, **2**, 492.

3 A. B. Murphy, P. R. F. Barnes, L. K. Randeniya, I. C. Plumb, I. E. Grey, M. D. Horne and J. A. Glasscock, *Int. J. Hydrogen Energy*, 2006, **31**, 1999.
4 (*a*) Y. Lin, S. Zhou, S. W. Sheehan and D. Wang, *J. Am. Chem. Soc.*, 2011, **133**, 2398; (*b*) G. Rahman and O.-S. Joo, *J. Mater. Chem. A*, 2013, **1**, 5554; (*c*) J. Jang, J. Lee, H. Ye, F. F. Fan and A. J. Bard, *J. Phys. Chem. C*, 2009, **113**, 6719; (*d*) D. Qin, C. Tao, S. In, Z. Yang, T. E. Mallouk, N. Bao and C. A. Grimes, *Energy Fuels*, 2011, **25**, 5257; (*e*) L. Wang, C. Y. Lee and P. Schmuki, *J. Mater. Chem. A*, 2013, **1**, 212; (*f*) I. Herrmann-Geppert, P. Bogdanoff, I. Radnik, S. Fengler, T. Dittrich and S. Fiechter, *Phys. Chem. Chem. Phys.*, 2013, **15**, 1389.
5 N. J. Cherepy, D. B. Liston, J. A. Lovejoy, H. M. Deng and J. Z. Zhang, *J. Phys. Chem. B*, 1998, **102**, 770.
6 A. J. Bosman and H. J. Van Daal, *Adv. Phys.*, 1970, **19**, 1.
7 J. Kennedy and K. Frese, *J. Electrochem. Soc.*, 1978, **125**, 709.
8 (*a*) I. Cesar, K. Sivula, A. Kay, R. Zboril and M. Grätzel, *J. Phys. Chem. C*, 2009, **113**, 772; (*b*) M. Barroso, S. R. Pendlebury, A. J. Cowan and J. R. Durrant, *Chem. Sci.*, 2013, **4**, 2724; (*c*) L. M. Peter, *J. Solid State Electrochem.*, 2013, **17**, 315.
9 F. Le Formal, N. Tetreault, M. Cornuz, T. Moehl, M. Grätzel and K. Sivula, *Chem. Sci.*, 2011, **2**, 737.
10 S. D. Tilley, M. Cornuz, K. Sivula and M. Grätzel, *Angew. Chem., Int. Ed.*, 2010, **49**, 6405.
11 M. Barroso, A. J. Cowan, S. R. Pendlebury, M. Grätzel, D. R. Klug and J. R. Durrant, *J. Am. Chem. Soc.*, 2011, **133**, 14868.
12 (*a*) K. Sivula, F. Le Formal and M. Grätzel, *Chem. Mater.*, 2009, **21**, 2862; (*b*) H. Dotan, O. Kfir, E. Sharlin, O. Blank, M. Gross, I. Dumchin, G. Ankonina and A. Rothschild, *Nat. Mater.*, 2013, **12**, 158.
13 (*a*) O. Zandi, J. A. Beardslee and T. Hamann, *J. Phys. Chem. C*, 2014, **118**, 16494; (*b*) P. Zhang, A. Kleiman-Shwarsctein, Y. S. Hu, J. Lefton, S. Sharma, A. J. Forman and E. McFarland, *Energy Environ. Sci.*, 2011, **4**, 1020; (*c*) T. Hisatomi, H. Dotan, M. Stefik, K. Sivula, A. Rothschild, M. Grätzel and N. Mathews, *Adv. Mater.*, 2012, **24**, 2699.
14 F. L. Souza, K. P. Lopes, E. Longo and E. R. Leite, *Phys. Chem. Chem. Phys.*, 2009, **11**, 1215.
15 I. Cesar, A. Kay, J. A. Gonzalez Martinez and M. Grätzel, *J. Am. Chem. Soc.*, 2006, **128**, 4582.
16 D. L. A. de Faria, S. Venaüncio Silva and M. T. de Oliveira, *J. Raman Spectrosc.*, 1997, **28**, 873.
17 Y. Y. Xu, D. Zhao, X. J. Zhang, W. T. Jin, P. Kashkarov and H. Zhang, *Phys. E*, 2009, **41**, 806.
18 (*a*) D. Bersani, P. P. Lottici and A. Montenero, *J. Raman Spectrosc.*, 1999, **30**, 355; (*b*) T. Yamashita and P. Hayes, *Appl. Surf. Sci.*, 2008, **254**, 2441.
19 L. A. Marusak, R. Messier and W. B. White, *J. Phys. Chem. Solids*, 1980, **41**, 981.
20 K. Itoh and J. O. Bockris, *J. Appl. Phys.*, 1984, **56**, 874.
21 P. Iwanski, J. S. Curran, W. Gissler and R. Memming, *J. Electrochem. Soc.*, 1981, **128**, 2128.
22 (*a*) L. Duan, L. Wang, A. K. Inge, A. Fischer, X. Zou and L. C. Chen, *Inorg. Chem.*, 2013, **52**, 7844; (*b*) P. W. Du, O. Kokhan, K. W. Chapman, P. J. Chupas and D. M. Tiede, *J. Am. Chem. Soc.*, 2012, **134**, 11096; (*c*) F. Jiao and H. Frei, *Energy Environ. Sci.*, 2010, **3**, 1018.
23 R. H. Goncalves, B. H. R. Lima and E. R. Leite, *J. Am. Chem. Soc.*, 2011, **133**, 6012.

